Temperature-Controlled Oxidation of $Ti_3C_2T_x$ MXene toward Fluorinated Anatase TiO_2 for Enhanced Photocatalytic Hydrogen Evolution

Nabilla Damayanti[1], Riki Subagyo[1], Saleha S. Maashi[3], Khawiyatur Riv'ah Agustina[1] , Hasliza Bahruji[2], David J. Morgan[3], Meenakshisundaram Sankar[3], Nurul Asikin-Mijan[4], Eko Santoso[1], Suprapto Suprapto[1], Reva Edra Nugraha[5], Atmanto Heru Wibowo[6], Didik Prasetyoko[1,*]

[1]*Department of Chemistry, Faculty of Science and Analytic Data, Institut Teknologi Sepuluh Nopember, Surabaya, 60111, Indonesia*

[2]*Centre of Advanced Material and Energy Science, Universiti Brunei Darussalam, Jalan Tungku Link, Gadong, 1410, BE, Brunei Darussalam*

[3]*Cardiff Catalysis Institute, Translational Research Hub, School of Chemistry, Cardiff University, Cardiff, CF24 4HQ*

[4]*Department of Chemical Sciences, Faculty of Science and Technology, Universiti Kebangsaan Malaysia, Bangi, 43600, UKM, Selangor Darul Ehsan, Malaysia*

[5]*Department of Chemical Engineering, Faculty of Engineering, Universitas Pembangunan Nasional "Veteran" Jawa Timur, Surabaya, East Java 60294, Indonesia*

[6]*Department of Chemitry, Faculty of Mathematics and Sciences, Universita Sebelas Maret, Surakarta, Indonesia*

**Corresponding author:* didikp@chem.its.ac.id

Abstract

In this study, TiO_2/MX composites were fabricated via controlled air calcination of $Ti_3C_2T_x$ MXene at 200-600 °C to tailor their phase composition and surface chemistry. The optimized TiO_2/MX5 photocatalyst (500 °C) achieved the highest H_2 production rate of 287 μmol g^{-1} h^{-1}, representing a 25.4 fold improvement over pristine MXene. The outstanding performance arises from a synergistic structural optimum combining high anatase crystallinity, preserved mesoporosity, abundant surface defects (I_D/I_G), and the retention of active Ti-F species, which collectively promote efficient charge separation and suppress carrier recombination. This work provides a simple and scalable strategy for engineering MXene-derived photocatalysts for solar-driven hydrogen production.

Keywords: $Ti_3C_2T_x$ MXene; Controlled oxidation; Surface fluorination; Anatase TiO_2, Photocatalytic hydrogen evolution

1. Introduction

Fossil fuels release greenhouse gases and harmful pollutants during combustion, significantly affecting air quality and worsening climate change. There is an urgent need to shift to renewable hydrogen, as hydrogen produces only water vapour during combustion, with no emissions of carbon dioxide or other greenhouse gases [1,2]. Utilisation of solar energy for the production of hydrogen via photocatalytic water splitting decomposes pure water into H_2 and O_2 in a 2:1 ratio. [3]. The generation of hydrogen (H_2) from water using photocatalysts converts solar energy into stored chemical energy, solving environmental pollution and the energy crisis [4]. However, commercialisation of the technology for photocatalytic water splitting is still hampered by low hydrogen production efficiency. Poor efficiency on photon scavenging and fast recombination of photoelectrons and holes before driving the redox reaction, converting the absorbed light energy into heat rather than chemical energy [5–7].

Titanium dioxide (TiO_2) is a stable and non-toxic photocatalyst for hydrogen production [8]. However, the wide band gap (3.2 eV) of TiO_2 limits light absorption in the UV region (5% of the solar spectrum), and rapid charge-carrier recombination further reduces efficiency [9]. Recently, multifunctional catalyst engineering strategies including defect engineering, surface functionalization, and heterostructure construction have been recognized as pivotal approaches to tailor electronic configurations, optimize intermediate adsorption, and lower kinetic barriers for high-efficiency hydrogen evolution and water splitting [10]. MXenes are derivatives of MAX phases that belong to a family of two-dimensional (2D) transition metal carbides, nitrides, and carbonitrides [11]. The general formula of $M_{n+1}X_nT_x$, where n = 1-3, refers to the number of atomic layers in a unit cell. M signifies the early transition metal (e.g., Nb, Ta, Cr, Sc, Ti, Zr, Mo, Hf, V, etc.), X denotes carbon, nitrogen, or both, and T_x represents the surface termination (hydroxyl,

58 oxygen, or fluorine) [12]. $Ti_3C_2T_x$ MXene exhibits high metallic conductivity with flexibility for
59 modification of the work function from 2 to 6 eV [13].
60 For photocatalysis, $Ti_3C_2T_x$ MXene was mainly used as a composite with other photocatalytic
61 materials and as a precursor for related photocatalysts. In addition to being used as a cocatalyst,
62 $Ti_3C_2T_x$ can be converted to TiO_2 with excellent photocatalytic properties in situ by calcination.
63 The outstanding charge storage performance and layered structure of $Ti_3C_2T_x$ endow it with the
64 ability to effectively restrain the recombination of electrons and holes in TiO_2 [14]. From a
65 theoretical standpoint, coupling semiconductor TiO_2 with metallic $Ti_3C_2T_x$ MXene constructs an
66 intimate metal semiconductor interface with strong electronic coupling. Driven by the work
67 function differential, photogenerated electrons are thermodynamically favored to migrate from the
68 conduction band of TiO_2 to the highly conductive MXene matrix, where MXene acts as an electron
69 sink to suppress electron-hole recombination. More importantly, the surface termination of
70 $Ti_3C_2T_x$, particularly Ti-F species, regulates the oxidation pathway during calcination and
71 influences the formation of the TiO_2/MXene heterointerface. The retained Ti-F bonds promote
72 strong interfacial electronic interactions and facilitate directional charge transport, providing a
73 theoretical basis for enhancing photocatalytic hydrogen evolution through controlled thermal
74 oxidation of MXene [15–17]. Previous studies have demonstrated that interfacial chemical bonds,
75 such as Ti-S bonds on TiO_2, can serve as efficient charge-transfer channels that accelerate carrier
76 separation in photocatalytic heterojunctions. By analogy, defect-rich TiO_2 derived from MXene is
77 expected to act as active pathways for charge transfer, thereby enhancing overall photocatalytic
78 activity [18].
79 In situ evolution of titanium dioxide (TiO_2) from Ti_3C_2 MXene establishes an atomic scale
80 interfacial heterostructure between TiO_2 and Ti_3C_2. The thermodynamically metastable edge

titanium atoms of Ti_3C_2 generate significant changes in Ti-electron orbitals during the oxidation process. Strong chemical bonds formed robust electronic interactions to facilitate the facile migration of charge carriers [19].

Although the thermal oxidation of $Ti_3C_2T_x$ MXene into TiO_2 has been investigated previously, most studies predominantly focus on simple phase transformations or complete oxidation, often overlooking the critical role of surface termination dynamics and defect evolution. Crucially, the explicit contribution of retained Ti-F species and their temperature-dependent interplay with surface defect states remain poorly understood**.** In this study, we demonstrate a controlled air calcination strategy to tailor the oxidation dynamics of $Ti_3C_2T_x$, creating a series of TiO_2/MX composites (200-600 °C). Unlike conventional approaches that attribute photocatalytic enhancements solely to surface area or bulk phase purity, we reveal a distinct relationship where the optimal 500 °C treatment (TiO_2/MX5) achieves a unique 'sweet spot'. This optimized condition unifies high bulk anatase crystallinity, preserved mesoporosity, maximum surface defect density (I_D/I_G), and strategic retention of active species. This work provides insights into the dual role of retained fluorine and defect states, establishing a clear design framework for MXene-derived photocatalysts beyond simple thermal conversion

2. Materials and Methods

2.1 Chemicals and precursors

Titanium aluminum carbide (Ti_3AlC_2, 98 %) and Hydrofluoric acid (HF) 40 % were purchased from Sigma Aldrich

2.2 Synthesis TiO_2 derived MXene

$Ti_3C_2T_x$ MXene was prepared from the MAX phase (Ti_3AlC_2, Nano-Research elements, > 99 %, APS < 40 μm) using an HF etching method previously reported in our group [20] . Specifically,

50 mL of a 40 % aqueous HF solution was poured into a 250 mL Teflon beaker in an ice bath. Then, 3g of Ti_3AlC_2 powder was gradually added to the HF solution. The mixture was stirred for 120 min, followed by sonication for 2h. The resulting solution was stored at room temperature for 24h under constant stirring. The resulting mixture was rinsed with a copious amount of deionised (DI) water until the pH reached approximately 6.5. The obtained MXene powder was then dried in a vacuum oven at 50 °C for 24 h.

The transformation of MXene into TiO_2 was achieved via thermal oxidation at different calcination temperatures. MXene powder was loaded into ceramic crucibles and calcined in a furnace at 200, 300, 400, 500, and 600 °C to induce oxidation.

2.3 Characterization

FTIR (Fourier Transform Infrared) Spectrophotometer Thermo Scientific Nicolet iS10 to determine the functional groups of the catalyst in the wave number range of 4000-400 cm^{-1}, X-ray Diffraction (XRD) X'pert PRO PANanalytical to determine the diffraction pattern of the catalyst with a scanning angle of 5-90° and the light source used for measurement is Cu Kα radiation (λ = 1.54060 Å), In order to characterize the textural properties of samples, Brunauer-Emmett-Teller (BET) surface analyses were performed using a Micromeritics TriStar Plus II PLUS instrument. The porosity of the samples was examined using N_2 adsorption-desorption method at 77 K. Before the measurement, all samples were degassed at 423 K for 4 h using the Micromeritics SmartPrep Programmable Degas System, The surface chemical composition and oxidation states of the samples were characterized by X-ray photoelectron spectroscopy (XPS) using a Thermo Scientific K-Alpha$^+$ spectometer equipped with a micro-focused monochromatic Al kα X-ray source operating at 72 W (6 mA × 12 kV). Data was collected over an elliptical area of approximately 400 x 600 μm^2 at pass energies of 50 and 150 eV for high-resolution and survey spectra,

respectively. Sample charging effects were minimised through a combination of low energy electron and Ar^+ ions. samples were prepared for analysis by pressing the powder on to double-sided adhesive tape attached to an IPA cleaned microscopy slide. Data was quantified using CasaXPS (v2.3.27) using Scofield sensitivity factors and an electron energy dependence according to the TPP-2M formulation. Due to changes in the nature of the surface an the interaction of the adventitious carbon with these surfaces, calibration was chosen to be against a signal for Ti(IV) in TiO_2, which is present in all samples; unlike pure bulk TiO2 (Ti $2p_{3/2}$ = 458.7 eV), the value was taken to be 459.6 eV for $TiO_{2-x}F_{2x}$ as discussed in [21] . All quantification was performed after calibration and subtraction of a Shirley background. Where applicable, peak fitting was achieved using Voigt-like functions defined by the LA line shape in CasaXPS taken from reference compounds (e.g. TiO_2), where lineshapes were unclear, spectra were interrogated using the informed amorphous sample model approach as used for Mo-oxides [22] and ceria [23] . . UV-DRS Spectrophotometer Shimadzu UV-2450 to measure the absorbance and reflectance of the catalyst in the wavelength range of 200-800 nm. The morphology was examined through FE-SEM, (Hitachi SU8200). High-resolution transmission electron microscopy (HR-TEM, Talos F200X) was used to analyze the sample surfaces.

2.4 Photocatalytic H_2 Production

H_2 photogeneration was carried out under visible light irradiation. 50 mg of sample was mixed with 25 mL of methanol solution 20 vol% in a 64 ml cylindrical quartz vial and covered using a rubber septum. The mixture was stirred for 10 min, followed by sonication treatment for 10 min. In order to remove the residual air, the mixture was purged with argon for 5 min. Subsequently, the mixture was placed in the photocatalytic reactor (Opsytec BS-02) equipped with Osram Powerstar light and a UV filter which provided visible light irradiation. At an hour intervals, 0.5

mL of the gas suspension was collected by gas syringe and analyzed using gas chromatography (GC, Shimadzu GC-2014) with a thermal conductive detector. The H_2 calibration was conducted according to the previous work in ref [24]. All experiments were performed three times to ensure reproducibility, results presented are the mean values with a total error of <5 %.

3. Result and Discussion

3.1 Structural and Morphological Characterization

The phase analysis of the samples was performed using XRD (Fig. 1a). Following the etching of the MAX phase with hydrofluoric acid (HF), the $Ti_3C_2T_x$ MXene exhibited XRD peaks at 2θ values of 8.94°, 18.36°, 27.41°, 35.74°, 41.52°, 48.91°, 56.27°, and 60.21° corresponding to the (002), (004), (108), (102), (105), (107), (108), and (110) diffraction planes [24]. After the oxidation, the characteristic at 2θ = 8.94° (002) peaks of $Ti_3C_2T_x$ MXene disappeared, whereas new TiO_2 peaks emerged and intensity increase with increasing oxidation temperature. After calcination at 200 °C (TiO_2/MX2), the MXene diffraction features are still dominant, with appearances of weak and broad TiO_2 peaks at 2θ = ~25°. Following calcination at 300-400 °C (TiO_2/MX3-TiO_2/MX4), well-defined diffraction peaks corresponding to anatase TiO_2 emerged at 2θ = ~25.03°, 37.5°, 48.1°, 54.0°, 55.1°, and 62.47° of anatase TiO_2 (JCPDS No. 00-021-1272) and some little peak of rutile TiO_2 at 2θ = 36° and 54.7° (JCPDS No. 00-021-1276). The disappearance of MXene diffraction peaks indicates the oxidation of Ti-C bonds into Ti-O frameworks. A slight peak shift at 25° anatase is observed, as shown in Fig. 1(b), which can be attributed to defects induced by Ti-F bonding. Anatase formation at intermediate temperatures suggests kinetically controlled oxidation, favoring the metastable anatase phase forms instead of the more stable rutile phase [25]. Upon increasing the calcination temperature to 500-600 °C (TiO_2/MX5-TiO_2/MX6), additional peaks attributed to rutile TiO_2 become evident, indicating a

phase transformation from anatase to the thermodynamically stable rutile phase. The coexistence of anatase and rutile phases at higher temperatures implies that MXene undergoes a polymorphic transformation. The oxidation and phase evolution of MXene into anatase and rutile TiO_2 demonstrates the potential of controlling the calcination temperature enable the tuning of crystalline phases of the composites. Ooxidation under a CO_2 atmosphere confirmed the coexistence of Ti_3C_2 based on the characteristic peak was still present below $2\theta = 10°$ [26]. Oxygen has a much higher oxidation potential than CO_2, which leads to the complete transformation of Ti_3C_2 into TiO_2 [27].

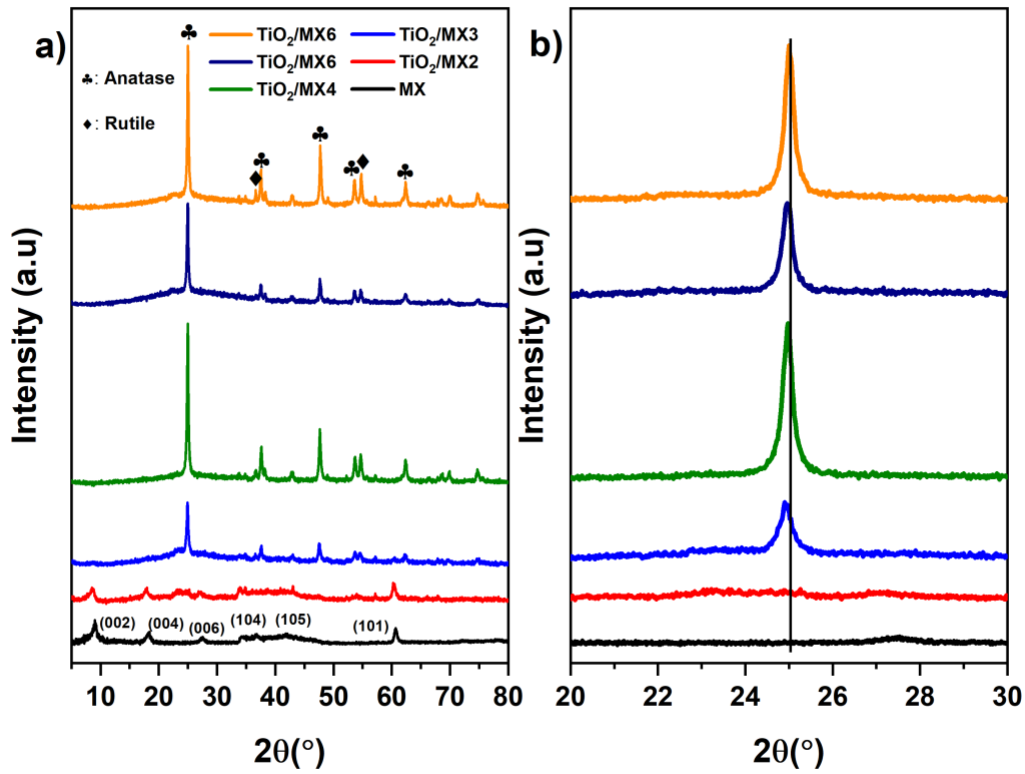

Fig. 1 (a) XRD patterns of the prepared TiO_2/MXene samples; (b) enlarged view in the 2θ range of 20-30°

FTIR spectra in Fig. 2(a,b) the MX sample shows a broad band at 3417 cm^{-1} attributed to O-H stretching, indicating hydroxyl groups or adsorbed water. A weak peak around 2857 cm^{-1} corresponds to CH_2 vibrations. Bands at 1614 cm^{-1} are assigned to Ti-OH , while peaks at 428 cm^{-1} confirm Ti-C bonds. Peaks at 563 cm^{-1} confirm C-C while peaks at 618 cm^{-1} confirm Ti-O. The presence of Ti-F at 740 cm^{-1} indicates fluorine terminations from the etching process. Peaks 1403 cm^{-1} confirm C-F, The C-F bond vibration in $Ti_3C_2T_x$ MXene originates from fluorine surface terminations at the defect sites (Ti vacancies) and flake edges [28,29]. After calcination (Fig. 2(c)) the band at 1000-400 cm^{-1} associated with the Ti-O-Ti vibration in all TiO_2 samples [30,31]. The bands at 1600 and 3500 cm^{-1} can be attributed to the bending vibration of the respective Ti-OH and -OH bond, and the stretching vibration of the water adsorbed OH group that gained intensity following air calcination [32]. The band at 2900 cm^{-1} assigned to stretching vibrations of the C-H bond and peaks at 3500 cm^{-1} that the intensity was gradually decreased following the calcination to 600^{o}C [33]. However, A small shoulder at 906 cm^{-1} observed (Fig. 2 (c)) after calcination at 600^{o}C is evidenced the formation of defects on TiO_2. This signal is associated with the stretching vibration of the Ti-F bond, indicating the presence of chemically adsorbed fluoride species on the TiO_2 surface [34].

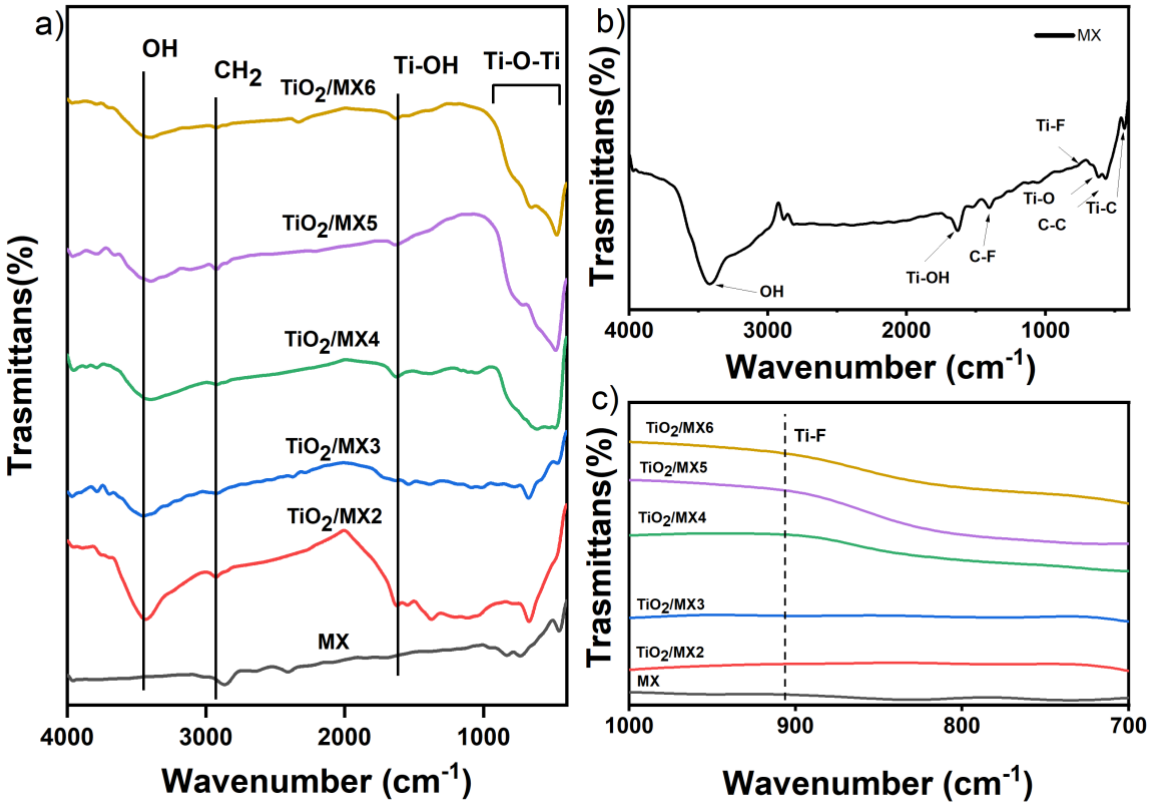

200

201 Fig. 2 (a) FTIR spectra of the prepared TiO_2/MXene samples; (b) enlarged view of pristine

202 MXene; (c) enlarged view of the Ti-F peak.

203 Fig. 3(a) displays the Raman spectra of pristine MXene and calcined samples. The pristine

204 MXene shows weak and broad Raman features of the metallic and layered structure. As shown in

205 the inset of Fig. 3(b), peaks at 128, 208, 380, 618, and 700 cm^{-1} correspond to Raman-active

206 vibration modes of $Ti_3C_2T_x$ MXene [35]. Raman peaks at 148 (E_g), 399 (B_{1g}), 518 (A_{1g} + B_{1g}), and

207 642 (E_g) cm^{-1} are characteristic optical modes of anatase TiO_2 were observed in TiO_2/MX4;

208 TiO_2/MX; TiO_2/MX5 [36]. For TiO_2/MX3 and TiO_2/MX2, the anatase peaks are remain weak,

209 indicating incomplete oxidation that transformed into amorphous TiO_2. The gradual evolution of

210 Raman features confirms a temperature-dependent crystallization process, transitioning from

211 poorly ordered oxide species to well-defined TiO_2. In addition, as shown in Fig. 3(d), a slight shift

of the Eg mode is observed, indicating the presence of structural defects in the anatase TiO_2. Pure TiO_2 displays the characteristic Eg mode centered at 143 cm^{-1}, corresponding to the symmetric stretching vibration of O-Ti-O bonds. Upon composite formation, the Eg mode exhibits a noticeable blue-shift to higher wavenumbers: 154 cm^{-1} ($\Delta\nu$ = +11 cm^{-1}) for TiO_2/MX4, 152 cm^{-1} ($\Delta\nu$ = +9 cm^{-1}) for TiO_2/MX5, and 148 cm^{-1} ($\Delta\nu$ = +5 cm^{-1}) for TiO_2/MX6

This prominent blue shift and peak broadening are attributed to the phonon confinement effect induced by oxygen vacancies/surface defects and localized lattice strain at theTiO_2/MXene interface. Notably, as the calcination temperature increases from 400 °C to 600 °C (TiO_2/MX4 to TiO_2/MX6), the Eg peak systematically shifts back toward lower wavenumbers. This quantitative shift reflects the thermal annealing of crystal defects and lattice strain relaxation at higher temperatures, which aligns consistently with the observed increase in crystallite size and crystallinity.

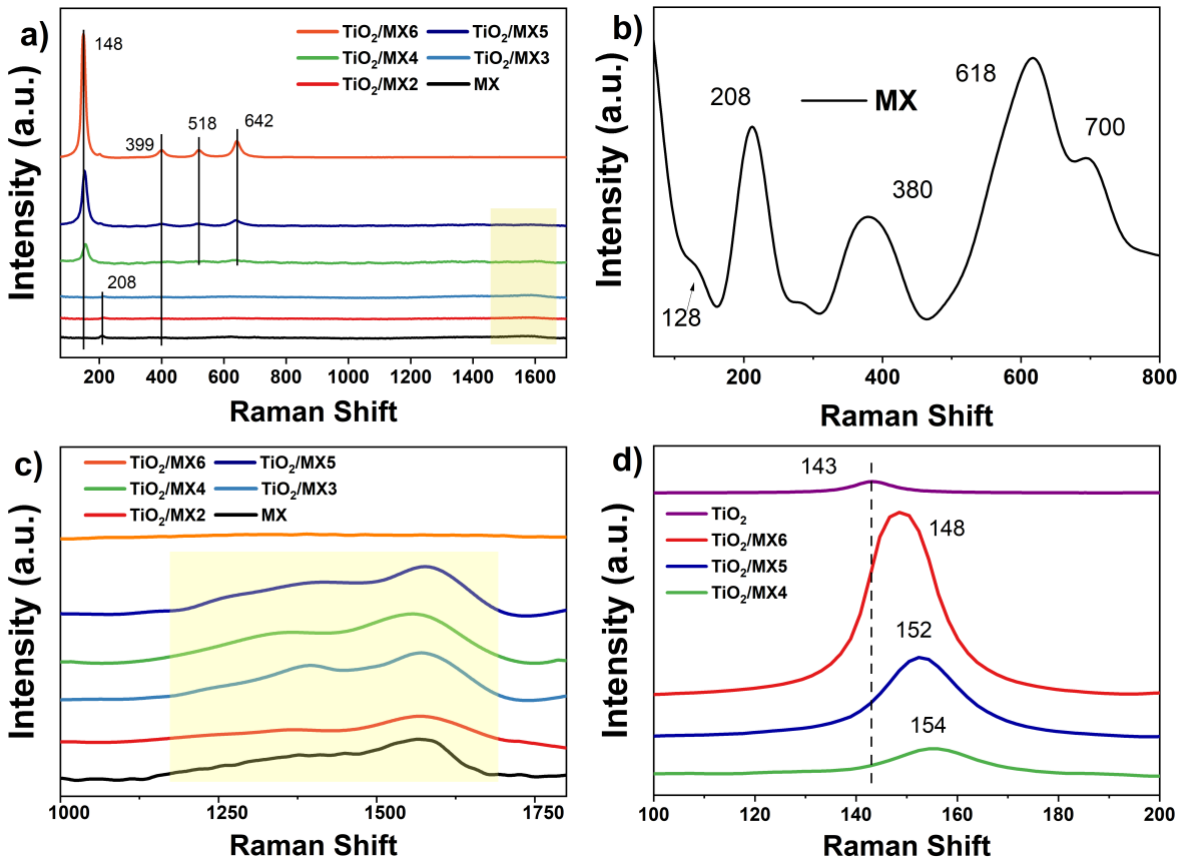

Fig. 3 Raman spectroscopic analysis of MXene-derived TiO_2/MX composites. (a) Full Raman spectra of pristine MXene and TiO_2/MX composites calcined at different temperatures; (b) characteristic Raman spectrum of pristine MXene; (c) enlarged D and G band region; and (d) enlarged anatase Eg vibrational mode.

TGA/DTG analysis in Fig. 4(a) exhibits three stages of weight loss at approximately 114, 184, and 405 °C. The initial weight loss in the range of 100-114 °C is attributed to the removal of intercalated and physically adsorbed water molecules from the MXene layers. The decomposition stage observed at ~ 184 °C is associated with the gradual evavuation of surface hydroxyl (-OH) terminations. A rapid mass increase occurring at temperatures above 405 °C indicates the onset of MXene oxidation. The oxidation of Ti_3C_2 in the presence of oxygen follows the stoichiometric reaction:

$$Ti_3C_2 + 5O_2 \rightarrow 3TiO_2 + 2CO_2 \quad (1)$$

The oxidation of 1 mol of Ti_3C_2 (167.6 g) leads to the formation of 3 mol of TiO_2 (3×79.9 g mol^{-1} = 239.7 g), resulting in a net mass gain. The oxidation of Ti_3C_2 is an exothermic process, which accounts for the pronounced mass increase at elevated temperatures [37,38]. This oxidation behavior is consistent with the XRD results, where characteristic diffraction peaks of TiO_2 begin to emerge in MXene samples calcined at 400 °C.

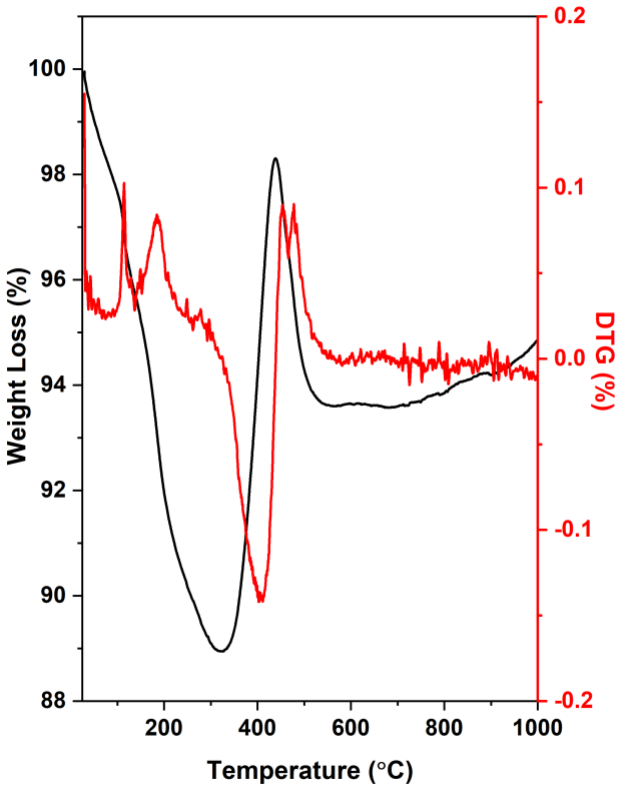

Fig. 4 TGA-DTG curves of pristine MXene.

The textural evolution induced by calcination is evidenced by N_2 adsorption-desorption analysis, as shown in Fig. 5(a-b). Pristine MXene exhibits a low surface area (5.28 m^2/g) due to its stacked morphology (Table 1). In contrast, calcined samples display type IV isotherms with H3 hysteresis loops, characteristic of mesoporous structures formed by aggregated plate-like particles. The surface area and pore volume increase significantly with temperature, reaching maximum values at 400 °C (TiO_2/MX4), with a surface area of 30.88 m^2/g and pore volume of 0.106 cm^3/g. At higher temperatures, a slight decrease in surface area is observed (e.g., 18.49 m^2/g for TiO_2/MX5), which can be ascribed to grain growth, sintering effects, and partial pore collapse associated with increased crystallinity and phase transformation [39].

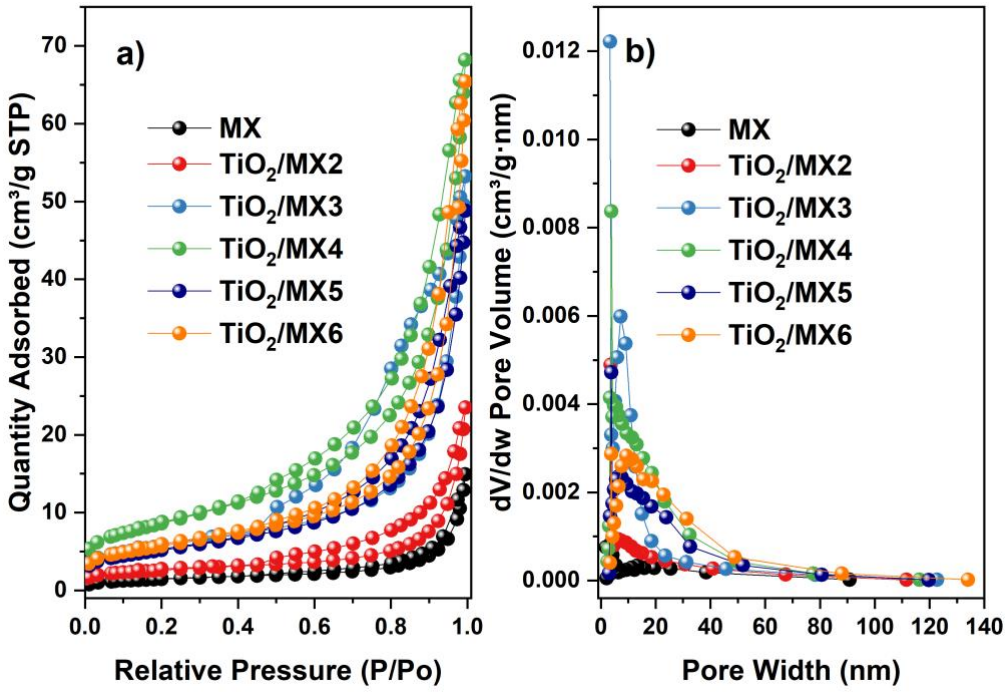

Fig. 5 N_2 adsorption-desorption analysis of calcined TiO_2/MX (a) isotherm (b) pore distribution.

Table. 1 Textural properties and optical band gap of TiO_2/MX samples

Sampel	Surface Area (m^2/g)				Pore Volume (cm^3/g)		Pore Diameter (nm)	Eg
	S_{BET}[a]	S_{meso}[b]	S_{micro}[c]	$S_{external}$[c]	V_{meso}[b]	V_{micro}[c]		
MX	5.28	4.83	0.39	4.88	0.022	0.0001	13.41	1.54
TiO_2/MX 2	9.33	9.84	2.55	6.78	0.036	0.001	14.62	1.44
TiO_2/MX 3	20.35	34.64	2.69	17.66	0.082	0.001	9.55	2.61
TiO_2/MX 4	30.88	34.12	2.48	28.4	0.106	0.0009	12.46	2.84
TiO_2/MX 5	18.49	20.95	1.87	16.61	0.075	0.0007	14.48	2.97
TiO_2/MX 6	20.43	22.82	1.9	18.53	0.101	0.0007	17.80	3.16

S_{BET} calculated by BET method

[b] S_{meso} and V_{meso} calculated by BJH method

[c] S_{mikro}, $S_{external}$, and V_{mikro} calculated by t-plot method

As shown in Fig. 6(a), MXene exhibits a layered structure composed of thin sheets. In Fig. 6(b), the TiO_2/MXene sample calcined at 500 °C shows a significantly disrupted layered structure, transforming into a rough, porous, and vertically fragmented morphology. The loss of well-defined lamellae at this temperature suggests the breakdown of Ti-C bonds and the collapse of the original MXene framework during its oxidation into TiO_2. TEM analysis (Fig. 6(c)) reveals that the oxidized sample consists of microcrystalline structures esembled into a non-uniform or poorly ordered matrix. High-resolution TEM images show distinct lattice fringes with interplanar spacings of approximately 0.356 nm and 0.325-0.326 nm, which can be indexed to the (101) plane

of anatase and the (110) plane of rutile TiO_2, respectively [39–42]. The coexistence of multiple lattice spacings within a single region suggests structural heterogeneity and lattice distortion in the TiO_2 framework. Such distortion is likely associated with the presence of residual Ti-F bonding inherited from the MXene surface terminations, which can modify the local electronic structure and induce lattice strain during the oxidation process. The retained fluorine species, as confirmed by XPS analysis, may influence crystal growth and contribute to defect formation within the TiO_2 lattice.

To further assess the structure of the optimal TiO_2/MX5, SAED analysis was performed (Fig. 6(d)). The diffraction rings are exclusively indexed to the (101), (004), (200), (105), (204), (116), (215), and (224) planes of anatase TiO_2 [43], confirming complete oxidation of the $Ti_3C_2T_x$ MXene at 500 °C. Thus, the enhanced H_2 evolution is not attributed to a residual TiO_2/MXene heterojunction, but rather to MXene-derived surface modification through retained TiF terminations and surface defects ($I_D/I_G = 0.699$), which may promote charge trapping and suppress electron-hole recombination.The EDS mapping (Fig. 6(e)) confirms the presence of Ti, O, and C as the major elements, with Ti and O dominating the composition, consistent with the formation of TiO_2. Elemental mapping images reveal a uniform spatial distribution of Ti and O throughout the material, indicating homogeneous oxidation rather than phase segregation. The residual carbon may enhance electrical conductivity and facilitate charge transport, which is beneficial for catalytic and photoelectrochemical applications [44,45].

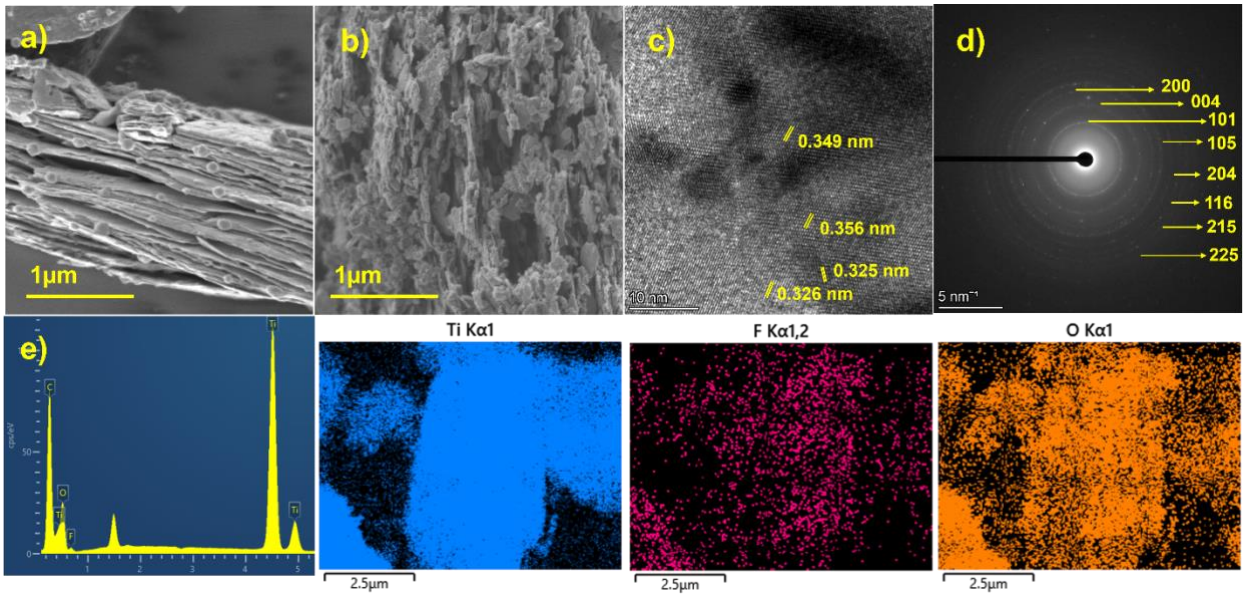

Fig. 6 (a) FESEM image of pristine MXene; (b) FESEM image of calcined TiO_2/MXene at 500°C; (c) TEM image of calcined TiO_2/MXene at 500 °C; (d) SAED pattern of calcined TiO2/MX at 500 °C; (e) EDX elemental mapping of calcined TiO_2/MXene at 500 °C.

3.2 Surface Chemical States of TiO_2/MX

X-ray photoelectron spectroscopy (XPS) analysis was performed on pristine MXene (MX) and TiO_2/MX samples calcined at different temperatures (200-600 °C) to investigate the evolution of surface elemental oxidation states (Fig. 7a-c).

The as-recvied $Ti_3C_2T_x$ MXene shows a characteristic asymetric C 1s signal, attirbutable to Ti-carbide, at 282.2 eV and consistent with a that reported by Natu *et al.* [21], but with significant levels of adventitious carbon (Fig 7a). Calcincation reveals the loss of the carbibe by 400 °C and is concominant with the complete conversion of the Ti 2p spectrum to that representative of TiO_2 indicating the complete structural transformation of $Ti_3C_2T_x$ into an oxide phase.

The corresponding Ti 2p spectra (Fig 7b) reveal a systematic oxidation towards TiO_2, with a loss of the Ti-C carbide (Ti $2p_{3/2}$ = 455.1 eV) phase by 400 °C. Of note is the initial Ti-oxide

309 (Ti_xO_y) and Ti-oxyfluoride like ($Ti_xO_yF_z$) components to the spectra. Nevertheless, the step wise
310 oxidation revelaes the systematic change to TiO_2, with signifcant levels of fluorine remaining, and
311 repsonsible for the higher binidng energy Ti(IV) state [21]. The fluorine (Fig 7c) reveals a shoft
312 from Ti-F bonds (685.3 eV) to more mixed, oxygen-fluorine like bonds (*ca*. 686 - 689 eV) and
313 consistent with the interpretation of the Ti and C signals, however we do not draw any further
314 conclusions from the F 1s data due to the probability of overlapping signals, and the presence of
315 residual AlF_x species from the preparaiton.

316 To inspect the surface oxygen species after calcination, the O 1s XPS spectra were deconvoluted
317 into three distinct components (Fig. S1 and Table S1): lattice oxygen (O_L) at 529.8 eV, surface
318 hydroxyl species (O_{OH}) at 531.1 - 531.7 eV, and chemisorbed water (O_{H_2O}) at 532.6 - 532.6 eV.As
319 summarized in Table S1, the relative ratio of surface hydroxyls to lattice oxygen (O_{OH}/O_L)varies
320 non-linearly with calcination temperature, exhibiting values of 0.243, 0.537 and 0.183 for
321 TiO_2/MX4, TiO_2/MX5, and TiO_2/MX6, respectively. The maximum observed for TiO_2/MX5
322 indicates a higher abundance of surface reactive hydroxyl groups that facilitate interfacial reactions
323 with adsorbed species.In accordance with the surface science principles established by Idriss [46],
324 ex-situ XPS O 1s signals in the 531-532 eV range cannot be unambiguously assigned to oxygen
325 vacancies, as ambient water exposure rapidly heals surface vacancies to form surface hydroxyls.
326 Therefore, the elevated O_{OH}/O_L ratio in TiO_2/MX5 is utilized as indirect evidence for defect-
327 mediated surface hydroxylation rather than direct proof of bulk oxygen vacancies.

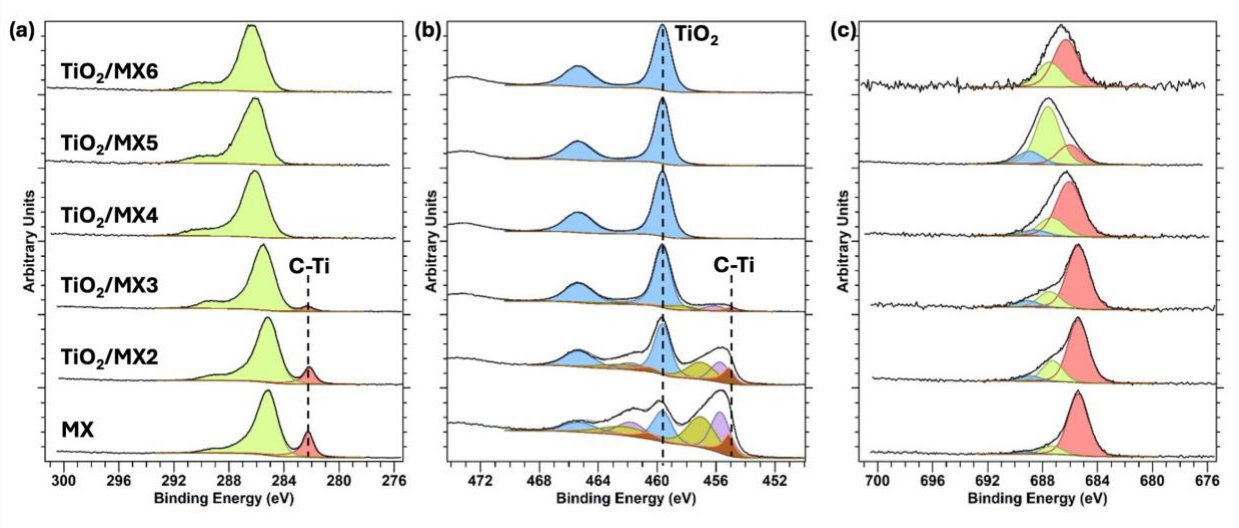

Fig. 7 XPS spectra of pristine MXene (MX) and TiO_2/MX calcined at different temperatures (a) C 1s, (b) Ti 2p, and (c) F 1s spectra. (Note: For clarity, the C 1s compnents of the adventious carbon are all coloured green, with the C-Ti peaks in red.)

XPS analysis of the fresh and spent TiO_2/MX5 catalyst after photocatalytic water splitting was conducted to investigate the surface chemical stability and electronic structure evolution (Fig. 8(a-c). The Ti 2p, C 1s and F 1s spectra of the spent catalyst are similar to the fresh catlayti, with only slight differneces in the rations of fluroide and oxygen species (O 1s not shown), and which we attribute to the prolonged interaction with water molecules and subsequent surface hydroxylation during photocatalysis, and would also be responsible for the the differences in the ratios of the F 1s components, with changes respresentative of the relative proportions of oxide/oxylurofide/hydroxides at the surface.. The retained Ti^{4+} peaks indicate that the TiO_2 structure remained stable after the reaction. No additional impurity peaks were observed, confirming the good chemical stability of the TiO_2/MX5 catalyst. XPS results suggest that the catalyst maintains its structural integrity after long-term photocatalytic water splitting, while the increased hydroxylation and defect-related surface species may contribute to sustained photocatalytic activity [47–49].

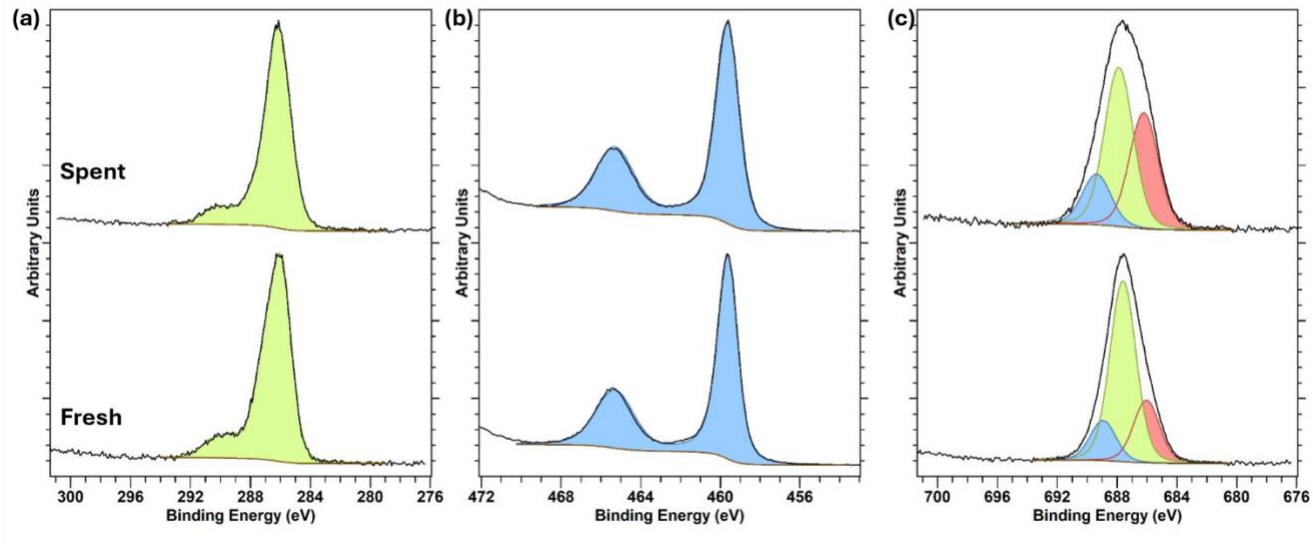

Fig. 8 XPS spectra of TiO_2/MX5 spent and TiO_2/MX5 fresh catalyst (a) C 1s, (b) Ti 2p, and (c) F 1s spectra

3.3 Optical analysis

The optical properties of as-prepared MXene and air-calcined TiO_2/MX samples were investigated by UV-Vis diffuse reflectance spectroscopy (DRS), Tauc analysis, Electrochemical Impedance Spectroscopy (EIS) and photoluminescence (PL) spectroscopy, as shown in Figure 9(a-d). Fig. 9(a) shows the UV-Vis absorption spectra of MX and TiO_2/MX samples. Pristine MX exhibits broad absorption over the entire UV-visible range, which is characteristic of its metallic nature and high free-carrier density. However, such broad absorption does not translate into photocatalytic activity due to the absence of a band gap and severe charge recombination. After calcination, the absorption behaviour changes significantly. TiO_2/MX2 and TiO_2/MX3 retain relatively strong absorbance in the visible light region, suggesting that incomplete oxidation generates a heterostructure between metallic MX and crystallised TiO_2. As the calcination temperature increases to 400-600 °C, an absorption edge emerges in the UV region, corresponding to the formation of TiO_2. TiO_2/MX5 shows a well-defined absorption edge while still maintaining

moderate visible-light absorption, which can be attributed to defect states from residual carbon and fluoride species. Defects in TiO_2 crystal structure enhanced the generation of oxygen vacancies for trapping of electrons and holes. In contrast, TiO_2/MX6 exhibits a sharper absorption edge and reduced visible absorption, suggesting increased crystallinity and reduced defect density at higher temperatures [50].

Fig. 9(b) presents the Tauc plots derived from UV-Vis diffuse reflectance spectra for pristine MXene and TiO_2/MX samples. The band gap gradually increases from MXene to TiO_2/MX obtained at higher temperatures. TiO_2/MX2 and TiO_2/MX3 exhibit relatively narrow band gap energy 1.44 and 2.61 Ev which implies the presence of sub-bandgap states following incomplete oxidation of MXene that instil structural disorder in TiO_2. At 400^{o}C and 500^{o}C calcination temperatures, the TiO_2/MX4 and TiO_2/MX5 the band gap were determined at 2.84 and 2.97 eV respectively, slightly narrowed compared to commercial anatase TiO_2 at 3.2 eV. The presence of Ti-F and carbon dopants may induce mid-gap states in TiO_2, as suggested by the shoulder observed in the UV-Vis spectra. TiO_2/MX6 shows a wider band gap energy of 3.01 eV among the samples, which can be attributed to higher crystallinity of TiO_2 from the reduced defect density, and partial rutile formation. Although a wider band gap can enhance charge mobility, the adsorption of photon in the visible light region is limited, compromising hydrogen production in TiO_2/MX6. Mild calcination temperatures produced TiO_2 with inherited Ti-F and carbon impurities, that red-shift the absorption edges to the visible light region [51].

To gain deeper insights into the charge transfer behavior of the hybrids, Electrochemical Impedance Spectroscopy (EIS) and Photoluminescence (PL) analyses were conducted (Fig. 9c-d). In the EIS Nyquist plots (Fig. 9c), the semicircle arc radius in the high-frequency region directly reflects the charge-transfer resistance at the catalyst interface. TiO_2/MX5 exhibits a substantially

smaller arc radius compared to bare MXene and other composites (e.g., TiO_2/MX4 and TiO_2/MX6), demonstrating a significantly reduced the charge-transfer resistance and faster interfacial charge transport [52]. This rapid electron migration behavior is further corroborated by the PL quenching observed in Fig. 9d. The marked decrease in emision intensity for TiO_2/MX5 reflects the efficient spatial separation of photogenerated electron hole pairs. The bare MXene exhibits the highest PL emission intensity, indicating a rapid recombination of photogenerated electron-hole pairs. Upon composite with TiO_2, the PL intensity decreases, with TiO_2/MX5 displaying the most significantly quenched emission. The lower PL intensity of TiO_2/MX5 indicates that these defect sites act as effective charge traps, thereby suppressing electron-hole recombination. These features facilitate the migration of photogenerated electrons to active sites for hydrogen evolution, in agreement with the superior hydrogen production rate observed in TiO_2/MX5 [53].

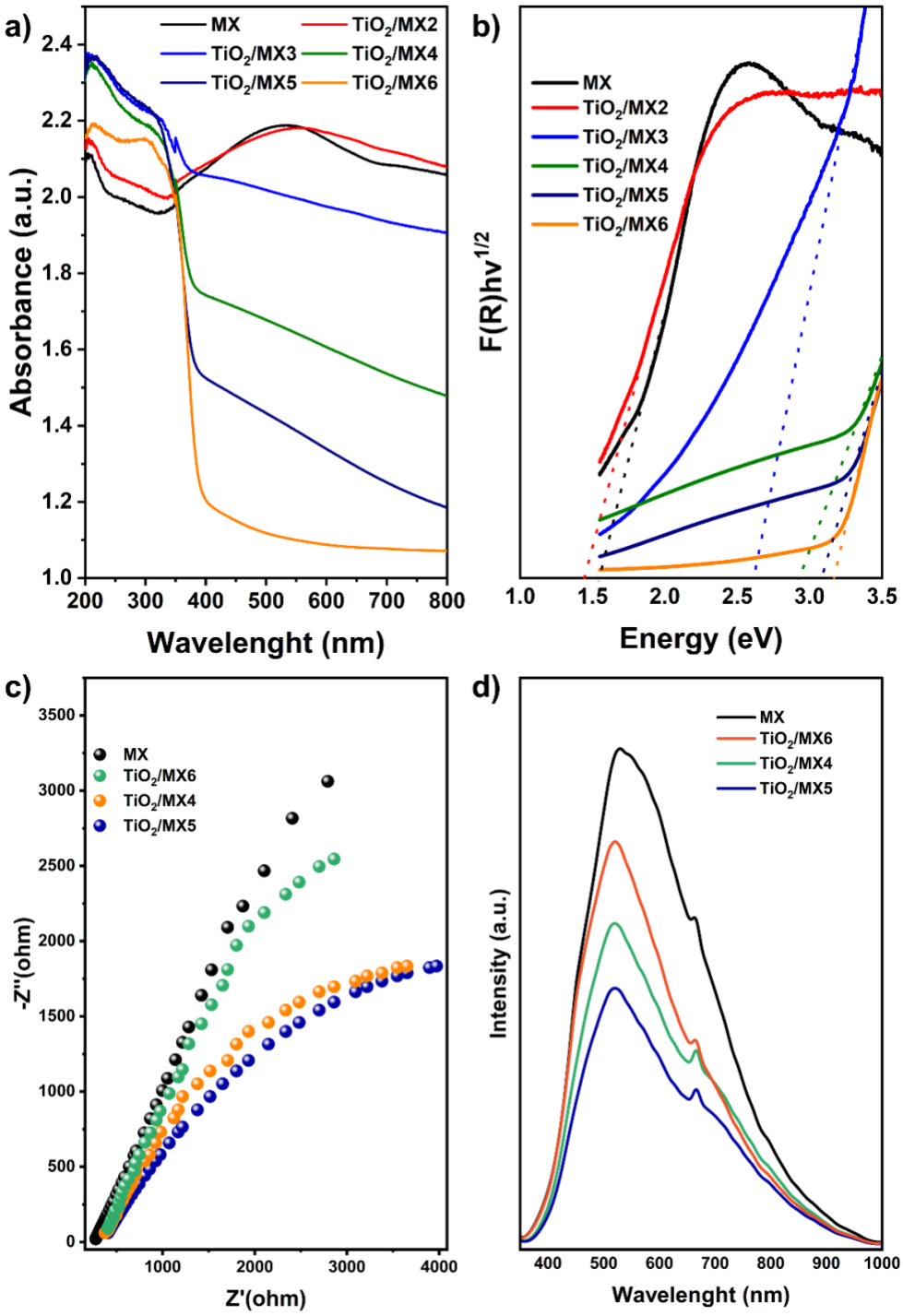

396

397 Fig. 9 Optical properties of MX and TiO_2/MX samples: (a) UV-Vis diffuse reflectance

398 spectra; (b) Tauc plots for band gap estimation; (c) Nyquist plots of selected samples; d)

399 photoluminescence spectra of selected samples.

3.4 Catalytic Activity

The photocatalytic hydrogen production of pristine MX and calcined TiO_2/MX samples was evaluated under UV-visible light irradiation, as shown in Fig. 10(a-c). The results demonstrate a strong dependence of hydrogen evolution activity on the calcination temperatures, which is closely correlated with the structural and chemical evolution of MXene-derived TiO_2.

As shown in Fig. 10(a), pristine MXene exhibits a low hydrogen production, which can be attributed to the metallic nature and rapid charge recombination. Conversion to TiO_2/MX2 and TiO_2/MX3 following oxidation at 200-300 °C is insufficient to enhance hydrogen production, despite evidence of Ti-O formation and UV-visible absorbance. Calcination of MXene at low temperatures produced heterostructured metallic MXene with poorly crystallised TiO_2 which presumably promotes non-radiative recombination pathways. In contrast, a pronounced enhancement in hydrogen evolution is observed for TiO_2/MX4 and TiO_2/MX5, with TiO_2/MX5 (500 °C) exhibiting the highest hydrogen production rate of approximately 285 μmol g^{-1} h^{-1}. The optimal balance between crystalline anatase formation, defect density, and mesoporous architecture enhances TiO_2 photocatalytic activity. Crystalline TiO2 ensures effective charge transport, while defects and heteroatoms inherited from MXene facilitate charge separation and surface redox reactions. Interestingly, further increasing the calcination temperature to 600 °C (TiO_2/MX6) leads to a noticeable decrease in hydrogen production. This decline is consistent with the reduced surface area, partial pore collapse, and increased rutile formation. Although rutile can contribute to heterojunction formation, excessive crystallisation and grain growth reduce the density of active sites and hinder mass transport, ultimately limiting photocatalytic efficiency.

The time-dependent hydrogen evolution behaviour of the optimal sample (TiO_2/MX5) is shown in Fig. 10(b). The hydrogen production rate increases linearly with reaction time, indicating stable photocatalytic activity. Fig. 10(c) illustrates the effect of sacrificial agents on hydrogen production. Methanol generates hydrogen evolution, significantly higher than ethanol and isopropanol. The differences in catalyst activity might be associated with decreased oxidation kinetics and increased steric hindrance from methanol to isopropanol. Methanol is the simplest alcohol and has a lower oxidation potential, efficiently scavenging photogenerated holes to suppress electron-hole recombination. The reduced activity observed with ethanol and isopropanol further confirms that hydrogen production is governed by interfacial charge-transfer kinetics rather than light absorption alone [54].

For overall water splitting, the conduction and valence band edges of a photocatalyst must exceeds the the H^+/H_2 (0 V) and O_2/H_2O (+1.23 V vs. SHE) redox potentials. Band gap energy of ~2.0 eV or higher will overcome kinetic and thermodynamic losses however, a band gap energy below 3 eV will enable visible-light utilisation [55]. TiO_2/MX5, with a band gap of 2.97 eV, meets the band gap energy threshold, providing sufficient redox driving force while maintaining responsiveness in the UV-visible region. The level of photocatalytic activity demonstrates enhancement upon forming the optimized hybrid architecture. The peak H_2 production rate of TiO_2/MX5 (285 μmol g^{-1} h^{-1}) represents a 25.4 fold increase over pristine MXene (11.5 μmol g^{-1} h^{-1}) and 3.4 fold increase over TiO_2/MX4 (84.62 μmol g^{-1} h^{-1}). This substantial increase highlights the synergistic contribution of both structural and electronic characteristics rather than the influence of a single material property. To clarify the individual roles of these parameters, a multivariable correlation analysis was performed (Fig. S2), mapping the photocatalytic H_2 production rate against crystallinity, specific surface area, defect ratio (I_D/I_G), and residual Ti-F

peak area. The correlation clearly demonstrates that no single factor governs the photocatalytic trend independently. While TiO_2/MX4 possesses the highest surface area (30.88 m^2/g) and TiO_2/MX6 exhibits the highest relative crystallinity, neither achieves the maximum H_2 production. Instead, the performance peaks at TiO_2/MX5 (285.40 μmol g^{-1} h^{-1}). This superior activity is driven by the global maximum of surface defect density (I_D/I_G = 0.699) working in synergy with well-preserved Ti-F species and balanced anatase crystallinity. At 600 °C (TiO_2/MX6), high-temperature annealing eradicates surface defects (I_D/I_G = 0) and destroys Ti-F terminations, causing a severe activity drop despite peak crystallinity. Thus, TiO_2/MX5 represents an optimal electronic and structural for hydrogen production.

The photocatalytic H_2 evolution performance of TiO_2/MX5 was further compared with previously reported TiO_2 and Ti_3C_2-based photocatalytic systems, as summarized in Table 2. The H_2 evolution rate of TiO_2/MX5 (285 μmol g^{-1} h^{-1}) significantly higher than conventional binary TiO_2/Ti_3C_2 composite (120 μmol g^{-1} h^{-1}) and unmodified Ti_3C_2 MXene (121 μmol g^{-1} h^{-1}). Notably, without incoporating expensive noble metal co-catalyst. TiO_2/MX5 outperforms Ru-modified heterostructure such as TiO_2-Ti_3C_2/Ru (235 μmol g^{-1} h^{-1}) as well multi component oxide systems like $SrTiO_3$/Ti_3C_2/TiO_2 (276 μmol g^{-1} h^{-1}). It is worth noting that higher H_2 production rates have been reported for certain metal-sulfide/MXene heterostructure, such as ZnS/Ti_3C_2 (502.6 μmol g-1 h-1), which benefit from the narrower intrinsic bandgap of ZnS and fast hole-scavenging kinetics in a lactic acid system. This difference highlights the importance of photocatalyst composition, heterojunction architecture, co-catalyst, sacrificial agent, and irradiation conditions in determining H_2 evolution performance. Therefore, TiO_2/MX5 demonstrates competitive H_2 production performance, achieving a higher rate than several TiO_2/MXene-based photocatalysts without requiring a noble-metal co-catalyst.

468 Table. 2 Comparison of the photocatalytic activities of the synthesized catalysts and others from

469 similar studies used in water splitting.

Photocatalyst system	H_2 Production Rate (μmol g^{-1} h^{-1}	Light Source	Co-Catalyst	Reactant & Sacraficial Agent	Ref
$SrTiO_3/Ti_3C_2/TiO_2$	276	300 W Xe lamp (λ > 300 nm)	0.1 wt% Rh, 0.05 wt% Cr_2O_3 and 0.05 wt% CoOOH	-	[56]
$BiVO_4$@$ZnIn_2S_4/Ti_3C_2$ MXene quantum dots (QDs)	102.67	300 W Xe lamp	-	-	[57]
ZnS/Ti_3C_2	502.6	300 W Xe lamp		lactic acid:water = 1:4	[58]
TiO_2/MXene Ti_3C_2	120	350 W Xe		10% of glycerinum aqueous solution	[16]
TiO_2-Ti_3C_2/Ru	235	300 W Xe lamp		10% methanol	[59]
TiO_2+0.25%Ru	1.61	150 W Hg lamp		Distilated water	[60]
TiO_2/CNFs	7.2	450 W (Xe lamp)		Distilled H_2O	[61]
$CuInS_2$-TiO_2	118	500 W Xe lamp		0.050 M Na_2S + 0.050 M Na_2SO_3 (10mL)	[62]
Ti_3C_2 Mxene	121	300 W Xe lamp	0.38 wt% Rh and 0.05 wt% Cr	DI	[3]
Triphase TiO_2	273	Sunlight		50 mL of glycerol + water, (5/95, v/v)	[63]
TiO_2/MX5	285	Visible light		Methanol	This work

470

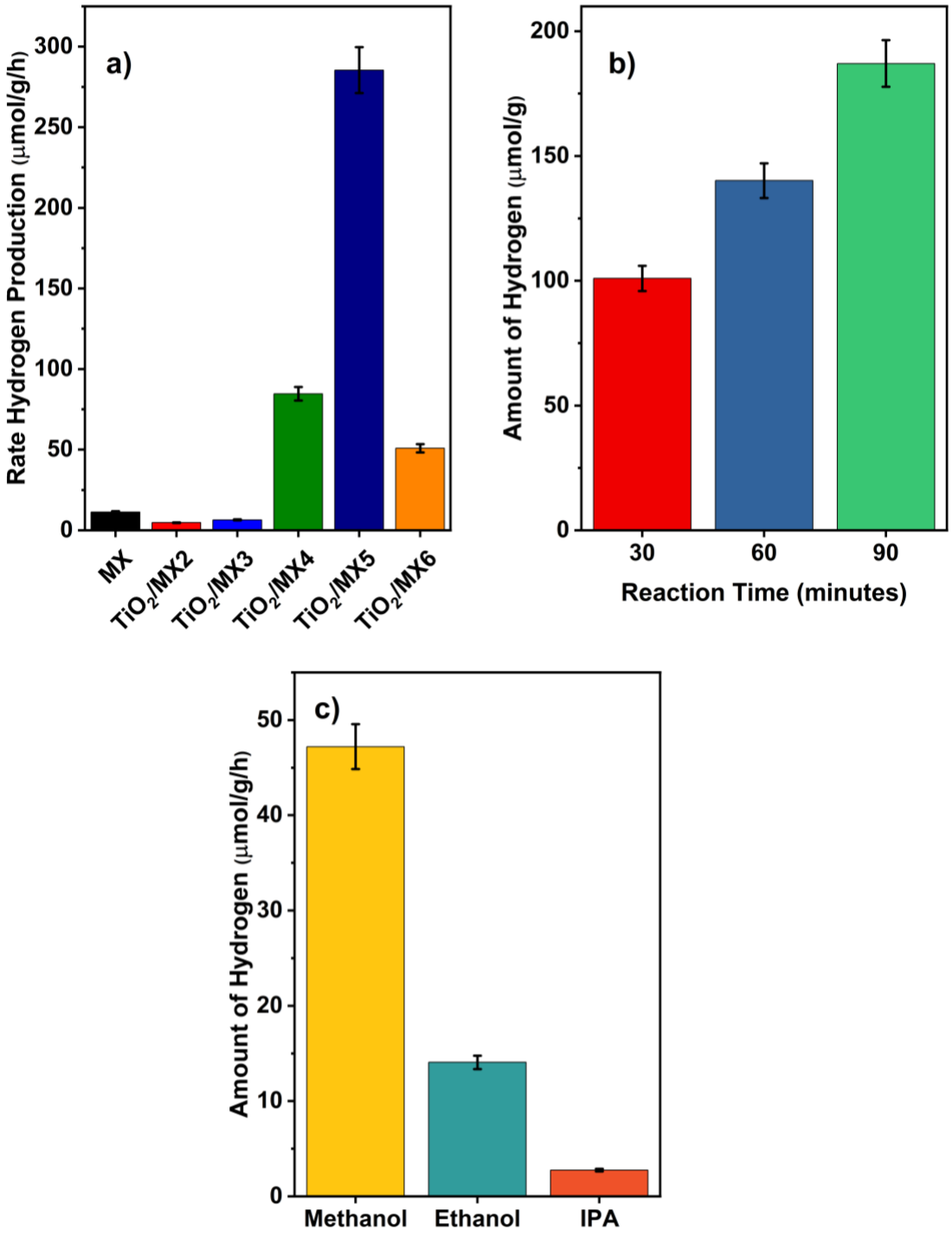

Fig. 10 Photocatalytic hydrogen evolution performance: (a) hydrogen production rates of MX and TiO_2/MX samples; (b) time-dependent hydrogen generation of TiO_2/MX5; (c) effect of sacrificial agents.

Conclusion

TiO_2/MX composites were successfully synthesized through controlled air calcination of $Ti_3C_2T_x$ MXene, demonstrating that calcination temperature is a key parameter in tailoring the phase composition and surface chemistry of MXene-derived photocatalysts. Among the prepared samples, TiO_2/MX5 (500 °C) exhibited the highest H_2 production rate of 287 μmol g^{-1} h^{-1}, corresponding to a 25.4 fold enhancement over pristine MXene. The superior photocatalytic performance originated from the synergistic combination of high anatase crystallinity, preserved mesoporosity, abundant surface defects (I_D/I_G), and retained Ti-F surface species, which collectively promoted efficient charge separation and suppressed carrier recombination. These findings provide a simple and scalable strategy for engineering the electronic and surface structures of MXene-derived TiO_2 photocatalysts for efficient solar-driven hydrogen production.

CRediT authorship contribution statement

Nabilla Damayanti: Investigation, Visualization, Writing - Original Draft. Riki Subagyo: Visualization, Formal analysis. Saleha S. Maashi: Visualization, Formal analysis. Khawiyatur Riv'ah Agustina: Visualization, Formal analysis. Hasliza Bahruji: Conceptualization, Writing - Review & Editing, David J. Morgan: Conceptualization, Writing - Review & Editing, Meenakshisundaram Sankar: Conceptualization, Writing - Review & Editing. Nurul Asikin-Mijan: Conceptualization, Writing - Review & Editing. Eko Santoso: Conceptualization, Writing - Review & Editing, Suprapto Suprapto: Conceptualization, Writing - Review & Editing. Didik Prasetyoko: Supervision, Writing - Review & Editing, Funding Acquisition.

Declaration of Competing Interest

The authors affirm that they do not possess any identifiable conflicting financial interests or personal ties that could have potentially influenced the findings presented in this paper.

Acknowledgment

The author from the Institut Teknologi Sepuluh Nopember gratefully acknowledges the Deputy for Research and Development, Ministry of Research and Technology of the Republic of Indonesia, for the research funding Kolaborasi Penelitian Strategis (Strategies Research Colaboration) through Grant Number 004/E5/E5/PG.02.00/PL.BATCH.2/2024 and local Grant Number 2644/PKS/ITS/2024. Additionally, the authors would like to express sincere gratitude to Dr. Sankar Meenakshisundaram from Cardiff University, United Kingdom, for reviewing this article and for serving as the host professor of the PKPI Scholarship Program.

Reference

[1] K. Ribag, Z. Mansouri, A. Al-Shami, I. Allaoui, O. Mounkachi, A. El Kenz, A. Benyoussef, Theoretical investigation of a van der waals SnS2/PtS2 heterostructure as a Z-scheme photocatalyst for efficient water splitting, J. Phys. Chem. Solids 208 (2026) 113134. https://doi.org/10.1016/j.jpcs.2025.113134.

[2] W. Zhang, J. Xiong, S. Li, W. Li, 1D-2D Z-scheme junction by coupling CaTiO3 rectangular nanorods with CdS nanosheets enhances photocatalytic hydrogen evolution, Mol. Catal. 570 (2025) 114701. https://doi.org/10.1016/j.mcat.2024.114701.

[3] X. Liu, Y. Mu, L. Shi, J. Yu, R. Tao, Z. Chu, S. Liu, X. Fan, K. Liu, Enhanced photocatalytic overall water splitting via Al-doped SrTiO3/Ti3C2 Mxene Schottky heterojunction, Int. J. Hydrogen Energy 170 (2025) 151173. https://doi.org/10.1016/j.ijhydene.2025.151173.

[4] S. Zong, J. Liu, Z. Huang, L. Liu, J. Liu, J. Zheng, Y. Fang, Mxene-TiO2 composite with exposed {101} facets for the improved photocatalytic hydrogen evolution activity, J. Alloys Compd. 896 (2022) 163039. https://doi.org/10.1016/j.jallcom.2021.163039.

[5] H.U. Mei, X.I.N. Jin, L.I.U. Zhenyu, Z. Hui, W. Yanze, Preparation of TiO 2 Supported Mxene Catalyst for High E fficiency Hydrogen P roduction, J. Wuhan Univ. Technol. 38 (2023) 286–291.

[6] O.F. Aldosari, I. Hussain, International Journal of Hydrogen Energy Unlocking the potential of TiO 2 -based photocatalysts for green hydrogen energy through water-splitting : Recent advances , future perspectives and techno feasibility assessment, Int. J. Hydrogen Energy 59 (2024) 958–981. https://doi.org/10.1016/j.ijhydene.2024.01.306.

[7] S.M. Thabet, H.N. Abdelhamid, S.A. Ibrahim, H.M. El Bery, Boosting photocatalytic water splitting of - TiO 2 using metal (Ru , Co , or Ni) co - catalysts for hydrogen generation, Sci. Rep. (2024) 1–10. https://doi.org/10.1038/s41598-024-59608-0.

[8] J.L. Aleksandra Pollap, Jarosław Serafin, Isabel Serrano, Joanna Sreńscek-Nazzal, Promising photocatalysts based on nanoshaped TiO 2 - rGO composite doped with metals (Pt and Cu) for hydrogen photoproduction, J. Environ. Chem. Eng. 10 (2022). https://doi.org/10.1016/j.jece.2022.108877.

[9] A. Pollap, J. Serafin, I. Serrano, J. Sreńscek-Nazzal, J. Llorca, Promising photocatalysts based on nanoshaped TiO2 - rGO composite doped with metals (Pt and Cu) for hydrogen photoproduction, J. Environ. Chem. Eng. 10 (2022) 108877. https://doi.org/10.1016/j.jece.2022.108877.

[10] S. Yuan, Y. Wang, H. Zhao, Z. Liu, Z. Liu, Z. Guo, R. Li, Multi-functional engineering of rare earth-based catalysts for high-efficiency water splitting, Energy Z 1 (2025) 1–38.

https://doi.org/10.20517/energyz.2025.04.

[11] M. Naguib, M. Kurtoglu, V. Presser, J. Lu, J. Niu, M. Heon, L. Hultman, Y. Gogotsi, M.W. Barsoum, Two-Dimensional Nanocrystals Produced by Exfoliation of Ti 3 AlC 2, Adv. Mater. 23 (2011) 4248–4253. https://doi.org/10.1002/adma.201102306.

[12] J. Serafin, B. Dziejarski, G. Oindo Achieng, X. Vendrell, S. Chaitoglou, R. Amade-Rovira, Comprehensive analysis of MAX phase and MXene materials for advanced photocatalysis, electrocatalysis and adsorption in hydrogen evolution and storage, J. Ind. Eng. Chem. 142 (2025) 18–33. https://doi.org/10.1016/j.jiec.2024.07.023.

[13] M. Downes, C.E. Shuck, B. McBride, J. Busa, Y. Gogotsi, Comprehensive synthesis of Ti3C2Tx from MAX phase to MXene, Nat. Protoc. 19 (2024) 1807–1834. https://doi.org/10.1038/s41596-024-00969-1.

[14] T. Zhao, X. Liu, L. Huai, R. Feng, T. Yan, W. Xu, Y. Zhao, Fabrication of the TiO2/Ti3C2 loaded ceramic membrane targeting for photocatalytic degradation of PPCPs: ciprofloxacin, tetracycline, and ibuprofen, Front. Environ. Sci. Eng. 18 (2024) 123. https://doi.org/10.1007/s11783-024-1883-5.

[15] N. García-Romeral, Á. Morales-García, F. Viñes, Effect of the Ti 2 CT x (T x = O, OH, and H) Functionalization on the Formation of (TiO 2) 5 /Ti 2 CT x Composites, J. Phys. Chem. C 129 (2025) 826–836. https://doi.org/10.1021/acs.jpcc.4c06909.

[16] Y. Li, D. Zhang, X. Feng, Y. Liao, Q. Wen, Q. Xiang, Truncated octahedral bipyramidal TiO 2 /MXene Ti 3 C 2 hybrids with enhanced photocatalytic H 2 production activity, Nanoscale Adv. 1 (2019) 1812–1818. https://doi.org/10.1039/C9NA00023B.

[17] P. Qiu, J. Xiong, M. Lu, L. Liu, W. Li, Z. Wen, W. Li, R. Chen, G. Cheng, Integrated p-n/Schottky junctions for efficient photocatalytic hydrogen evolution upon Cu@TiO2-Cu2O

ternary hybrids with steering charge transfer, J. Colloid Interface Sci. 622 (2022) 924–937. https://doi.org/10.1016/j.jcis.2022.04.107.

[18] W. Yu, G. Cheng, W. Li, Y. Wei, C. Han, J. Xiong, Integrating S-Scheme Heterojunction with Interfacial Metal-Sulfur Bonds Promotes Solar-to-Hydrogen Evolution in TiO 2 @Pd-Doped ZnIn 2 S 4 Core@Shell Photocatalysts, Adv. Funct. Mater. 36 (2026). https://doi.org/10.1002/adfm.76688.

[19] B.P. Mishra, L. Biswal, S. Das, L. Acharya, K. Parida, Architecture and Kinetic Studies of Photocatalytic H 2 O 2 Generation and H 2 Evolution through Regulation of Spatial Charge Transfer via Z - Scheme Path over a (001) Facet Engineered TiO 2 @ MXene / B - g - C 3 N 4 Ternary Hybrid, Langmuir (2023). https://doi.org/10.1021/acs.langmuir.2c02315.

[20] N. Damayanti, D. Prasetyoko, S. Suprapto, R. Tamim, R. Subagyo, L. Kusnawati, N. Asikin-Mijan, R. Yusop, H. Holilah, A.A. Jalil, Pluronic P123 modified MXene as an efficient adsorbent for aqueous dye Removal: Optimization using CCD-RSM, J. Ind. Eng. Chem. 154 (2026) 557–573. https://doi.org/10.1016/j.jiec.2025.07.022.

[21] V. Natu, M. Benchakar, C. Canaff, A. Habrioux, S. Célérier, M.W. Barsoum, A critical analysis of the X-ray photoelectron spectra of Ti3C2Tz MXenes, Matter 4 (2021) 1224–1251. https://doi.org/10.1016/j.matt.2021.01.015.

[22] J. Baltrusaitis, B. Mendoza-Sanchez, V. Fernandez, R. Veenstra, N. Dukstiene, A. Roberts, N. Fairley, Generalized molybdenum oxide surface chemical state XPS determination via informed amorphous sample model, Appl. Surf. Sci. 326 (2015) 151–161. https://doi.org/10.1016/j.apsusc.2014.11.077.

[23] D.J. Morgan, Photoelectron spectroscopy of ceria: Reduction, quantification and the myth of the vacancy peak in XPS analysis, Surf. Interface Anal. 55 (2023) 845–850.

https://doi.org/10.1002/sia.7254.

[24] F. Saman, H. Bahruji, A.H. Mahadi, C.H.S. Ling, Pd/g-C3N4 photocatalyst for hydrogen production: Role of experimental condition for Schottky barrier, Fuel 349 (2023) 128725. https://doi.org/10.1016/j.fuel.2023.128725.

[25] C.-F. Li, Z.-Y. Hu, W. Li, Y. Li, B.-L. Su, Direct observation of the TiO2 anatase-rutile phase transition by in-situ transmission electron microscopy, Mater. Charact. 227 (2025) 115226. https://doi.org/10.1016/j.matchar.2025.115226.

[26] K. Chen, K. Yan, Q. Xie, H. Zhu, X. Li, Z. Dong, MXene-derived C-doped TiO2/Ti3C2 heterojunction as a high-performance visible-light photocatalyst, Res. Chem. Intermed. 48 (2022) 4443–4458. https://doi.org/10.1007/s11164-022-04830-6.

[27] Z. Liang, R. Khanna, K. Li, F. Guo, Y. Ma, H. Zhang, Y. Bu, Impact of oxidants O 2 , H 2 O , and CO 2 on graphene oxidation : A critical comparison of reaction kinetics and gasification behavior, Chem. Eng. J. 450 (2022) 138045. https://doi.org/10.1016/j.cej.2022.138045.

[28] T. Parker, D. Zhang, D. Bugallo, K. Shevchuk, M. Downes, G. Valurouthu, A. Inman, B. Chacon, T. Zhang, C.E. Shuck, Y.-J. Hu, Y. Gogotsi, Fourier-Transform Infrared Spectral Library of MXenes, Chem. Mater. 36 (2024) 8437–8446. https://doi.org/10.1021/acs.chemmater.4c01536.

[29] V.S. Bhat, S.B. Kapatkar, I. Naik, S. Hegde, Optical, electrical, structural properties by of PFO-PMMA films loaded with TiO2 nanoparticles, Discov. Mater. 4 (2024) 50. https://doi.org/10.1007/s43939-024-00124-3.

[30] R. Subagyo, G. Rizky Anindika, D.I. Utami, W.S. Sarifuddin, L. Zhang, S. Jovita, K.R. Agustina, N.A. Mijan, Y. Zetra, H. Bahruji, D. Suhendar, F.A.N. Mawaddah, D.

Prasetyoko, S.Z. Bisri, Arramel, Y. Kusumawati, Dendritic Fibrous Nano Silica–Titania for High-Performance Photocatalytic Hydrogen Evolution, ACS Appl. Energy Mater. 8 (2025) 1598–1608. https://doi.org/10.1021/acsaem.4c02742.

[31] N. Sondezi, Z. Njengele-Tetyana, K.P. Matabola, T.A. Makhetha, Sol–Gel-Derived TiO 2 and TiO 2 /Cu Nanoparticles: Synthesis, Characterization, and Antibacterial Efficacy, ACS Omega 9 (2024) 15959–15970. https://doi.org/10.1021/acsomega.3c09308.

[32] F. Zhang, W. Liu, S. Wang, H. Shi, Insight into anticorrosion / thermal stability behavior of protection system composed of waterborne polyurethane containing SiO x / TiO 2 @ Ti 3 C 2, (2021) 19840–19856. https://doi.org/10.1007/s10853-021-06468-y.

[33] B. Zewde, P. Pitliya, D. Raghavan, The role of surface modified TiO 2 nanoparticles on the mechanical and thermal properties of CTBN toughened epoxy nanocomposite, J. Mater. Sci. 51 (2016) 9314–9329. https://doi.org/10.1007/s10853-016-0179-y.

[34] C. Castañeda, F. Tzompantzi, R. Gómez, Photocatalytic reduction of 4-nitrophenol on in situ fluorinated sol–gel TiO2 under UV irradiation using Na2SO3 as reducing agent, J. Sol-Gel Sci. Technol. 80 (2016) 426–435. https://doi.org/10.1007/s10971-016-4104-2.

[35] B. Silva, S.S. Nemala, S. Kaushik, P.D. Silva, L. Saini, M. Barreiros dos Santos, B. Espiña, S. Marras, L.-H. Yeh, G. Kalon, A. Capasso, Sustainable MXene membranes for ion sieving and antibacterial water purification, J. Memb. Sci. 747 (2026) 125298. https://doi.org/10.1016/j.memsci.2026.125298.

[36] X. Vendrell, B. Dziejarski, R. Amade, L. Mestres, I. Serrano, J. Llorca, International Journal of Hydrogen Energy Synergistic enhancement of solar-driven hydrogen evolution via Ni-doped TiO 2 – MXene hybrid photocatalyst, 179 (2025). https://doi.org/10.1016/j.ijhydene.2025.151722.

[37] N. Liu, Q. Li, H. Wan, L. Chang, H. Wang, J. Fang, T. Ding, Q. Wen, L. Zhou, High-temperature stability in air of Ti 3 C 2 T x MXene-based composite with extracted bentonite, Nat. Commun. (2022) 1–10. https://doi.org/10.1038/s41467-022-33280-2.

[38] H. Pazniak, I.A. Plugin, M.J. Loes, T.M. Inerbaev, I.N. Burmistrov, M. Gorshenkov, J. Polcak, A.S. Varezhnikov, M. Sommer, D. V Kuznetsov, M. Bruns, F.S. Fedorov, N.S. Vorobeva, A. Sinitskii, V. V Sysoev, Partially Oxidized Ti3C2Tx MXenes for Fast and Selective Detection of Organic Vapors at Part-per-Million Concentrations, ACS Appl. Nano Mater. (2020). https://doi.org/10.1021/acsanm.9b02223.

[39] M.G. Kim, J.M. Kang, J.E. Lee, K.S. Kim, K.H. Kim, M. Cho, S.G. Lee, Effects of Calcination Temperature on the Phase Composition , Photocatalytic Degradation , and Virucidal Activities of TiO 2 Nanoparticles, ACS Omega (2021). https://doi.org/10.1021/acsomega.1c00043.

[40] C. Qiu, J. Shen, J. Lin, D. Li, J. Zhang, Z. Zhang, H. Lin, X. Wang, X. Fu, Construction of the Rutile/Anatase Micro-Heterophase Junction Photocatalyst from Anatase by Liquid Nitrogen Quenching Method, ACS Appl. Energy Mater. (2021). https://doi.org/10.1021/acsaem.1c02066.

[41] N. Shabana, P. Muhsin, Y. Yang, P. Chou, Anatase-Rutile TiO 2 @ V 4 C 3 T x MXene for Omnidirectional Electrocatalytic Water Splitting, Adv. Mater. Interfaces 2400597 (2025) 1–11. https://doi.org/10.1002/admi.202400597.

[42] S. Zhou, L. Jiang, H. Wang, J. Yang, X. Yuan, H. Wang, Oxygen Vacancies Modified TiO 2 / O-Terminated Ti 3 C 2 Composites : Unravelling the Dual Effects between Oxygen Vacancy and High-Work-Function Titanium Carbide, Adv. Funct. Mater. 2307702 (2023) 1–13. https://doi.org/10.1002/adfm.202307702.

[43] S. Ahmed, M.K.H. Shishir, M.T. Islam, M.A. Rahaman, S. Aman, A.R. Aidid, S.I. Sadia, M.M. Rana, M.A. Alam, Crystallinity integration of anatase (TiO2) nanocrystal by whole powder pattern fitting (WPPF) method: A Rietveld refinement study, Results Mater. 26 (2025) 100673. https://doi.org/10.1016/j.rinma.2025.100673.

[44] M. Boomhendi, M. Vatani, Y. Zare, M.T. Munir, Predictive modeling of conductivity for carbon black nanocomposites : influence of filler features , interfacial effects and network portion, Sci. Reportse (2026) 1–12.

[45] O. Mukhan, J. Yun, H. Munakata, K. Kanamura, S. Kim, Quantification of the Carbon-Coating Effect on the Interfacial Behavior of Graphite Single Particles, ACS Omega (2024). https://doi.org/10.1021/acsomega.3c08681.

[46] H. Idriss, On the wrong assignment of the XPS O1s signal at 531–532 eV attributed to oxygen vacancies in photo- and electro-catalysts for water splitting and other materials applications, Surf. Sci. 712 (2021) 2–7. https://doi.org/10.1016/j.susc.2021.121894.

[47] D. Bae, B. Seger, O. Hansen, P.C.K. Vesborg, I. Chorkendorff, Durability Testing of Photoelectrochemical Hydrogen Production under Day/Night Light Cycled Conditions, ChemElectroChem 6 (2019) 106–109. https://doi.org/10.1002/celc.201800918.

[48] C. Shuai, C. Kong, Y. Li, L. Zhang, C. Qi, Z. Mo, 3D flower-like bimetallic Ni–Co metal–organic framework as an electrocatalyst for the oxygen evolution reaction, RSC Adv. 14 (2024) 18367–18372. https://doi.org/10.1039/D4RA02280G.

[49] G. Helal, Z. Xu, W. Zuo, Y. Yu, J. Liu, H. Su, J. Xu, H. Li, G. Cheng, P. Zhao, Electrochemical water splitting enhancement by introducing mesoporous NiCoFe-trimetallic phosphide nanosheets as catalysts for the oxygen evolution reaction, RSC Adv. 14 (2024) 17202–17212. https://doi.org/10.1039/D4RA02344G.

[50] M. Li, W. Zhang, Y. Geng, B. Lu, J. He, J. Liu, X. Li, Enhanced Salinity Gradient Energy Conversion by Photodegradable MXene / TiO 2 Membrane Utilizing Saline Dye Wastewater, Adv. Funct. Mater. 2414342 (2025) 1–11. https://doi.org/10.1002/adfm.202414342.

[51] V.D. Eidsvåg H, Bentouba S, Vajeeston P, Yohi S, TiO 2 as a Photocatalyst for Water Splitting—An Experimental and Theoretical Review, Molecules (2021) 1–30.

[52] J. Serafin, X. Vendrell, B. Dziejarski, R. Amade, L. Mestres, I. Serrano, J. Llorca, Synergistic enhancement of solar-driven hydrogen evolution via Ni-doped TiO2–MXene hybrid photocatalyst, Int. J. Hydrogen Energy 179 (2025) 151722. https://doi.org/10.1016/j.ijhydene.2025.151722.

[53] X. Vendrell, B. Dziejarski, R. Amade, L. Mestres, I. Serrano, J. Llorca, International Journal of Hydrogen Energy Synergistic enhancement of solar-driven hydrogen evolution via Ni-doped TiO 2 – MXene hybrid photocatalyst, Int. J. Hydrogen Energy 179 (2025). https://doi.org/10.1016/j.ijhydene.2025.151722.

[54] Y. Wei, G. Cheng, J. Xiong, J. Zhu, Y. Gan, M. Zhang, Z. Li, S. Dou, Synergistic impact of cocatalysts and hole scavenger for promoted photocatalytic H2 evolution in mesoporous TiO2NiS hybrid, J. Energy Chem. 32 (2019) 45–56. https://doi.org/10.1016/j.jechem.2018.05.013.

[55] S. Nishioka, F.E. Osterloh, X. Wang, T.E. Mallouk, K. Maeda, Photocatalytic water splitting, Nat. Rev. Methods Prim. 0123456789 (2023) 1–15. https://doi.org/10.1038/s43586-023-00226-x.

[56] M. Cai, Y. Chen, Z. Zhuo, Y. Lu, S.S.A. Shuaib, Y. Jiang, J. Bai, Y. Wei, S. Sun, Construction of SrTiO3/Ti3C2/TiO2 Z-scheme derived from multilayer Ti3C2 MXene for

efficient photocatalytic overall water splitting, J. Alloys Compd. 1010 (2025) 177550. https://doi.org/10.1016/j.jallcom.2024.177550.

[57] X. Du, T. Zhao, Z. Xiu, Z. Xing, Z. Li, K. Pan, S. Yang, W. Zhou, BiVO4@ZnIn2S4/Ti3C2 MXene quantum dots assembly all-solid-state direct Z-Scheme photocatalysts for efficient visible-light-driven overall water splitting, Appl. Mater. Today 20 (2020) 100719. https://doi.org/10.1016/j.apmt.2020.100719.

[58] L. Tie, S. Yang, C. Yu, H. Chen, Y. Liu, S. Dong, J. Sun, J. Sun, In situ decoration of ZnS nanoparticles with Ti3C2 MXene nanosheets for efficient photocatalytic hydrogen evolution, J. Colloid Interface Sci. 545 (2019) 63–70. https://doi.org/10.1016/j.jcis.2019.03.014.

[59] Y. Liu, Y.-H. Li, X. Li, Q. Zhang, H. Yu, X. Peng, F. Peng, Regulating Electron–Hole Separation to Promote Photocatalytic H 2 Evolution Activity of Nanoconfined Ru/MXene/TiO 2 Catalysts, ACS Nano 14 (2020) 14181–14189. https://doi.org/10.1021/acsnano.0c07089.

[60] J. Kapica-Kozar, E. Kusiak-Nejman, K. Sobczuk, A. Wanag, W. Bednarski, K. Ćmielewska, E. Ekiert, I. Pełech, D. Sibera, P. Staciwa, M. Gano, U. Narkiewicz, A.W. Morawski, Ruthenium-modified TiO2 photocatalysts for hydrogen generation from water splitting and simultaneous CO2 photoreduction, J. Photochem. Photobiol. A Chem. 468 (2025) 116477. https://doi.org/10.1016/j.jphotochem.2025.116477.

[61] N. Nyamai, T. Phaahlamohlaka, Significantly advanced hydrogen production via water splitting over Zn/TiO2/CNFs and Cu/TiO2/CNFs nanocomposites, J. Ind. Eng. Chem. 134 (2024) 312–326. https://doi.org/10.1016/j.jiec.2023.12.061.

[62] M. Inada, S. Yase, A. Tada, T. Yamane, Y. Miyaji, M. Hirahara, Y. Harada, S. Fujii, T.

Fukushima, S. Dohshi, S. Higashimoto, Effect of the indium sulfide phase in CuInS2-TiO2 photocatalysts to boost hydrogen evolution by water splitting, Mater. Today Catal. 7 (2024) 100080. https://doi.org/10.1016/j.mtcata.2024.100080.

[63] A.D.G. Kafadi, H.Y. Hafeez, J. Mohammed, C.E. Ndikilar, A.B. Suleiman, Triphase TiO2 and N-doped g-C3N4 Photocatalysts Enhanced by Ti3C2Tx MXene for Photocatalytic Solar Fuel (H2) Production via Water Splitting, J. Mol. Struct. 1342 (2025) 142749. https://doi.org/10.1016/j.molstruc.2025.142749.